



Article

Natural Silkworm Cocoon-Derived Separator with Na-Ion De-Solvated Function for Sodium Metal Batteries

Zhaoyang Wang¹ , Zihan Zhou¹, Xing Gao¹, Qian Liu¹, Jianzong Man¹, Fanghui Du¹ and Fangyu Xiong^{2,3,*} 

¹ Shandong Provincial Key Laboratory of Chemical Energy Storage and Novel Cell Technology, College of Chemistry Engineering, Liaocheng University, Liaocheng 252059, China; wzy9218@126.com (Z.W.); 13884971808@163.com (Z.Z.); 18764892075@163.com (X.G.); 13562862100@163.com (Q.L.); manjianzong@lcu.edu.cn (J.M.); dufanghui@lcu.edu.cn (F.D.)

² College of Materials Science and Engineering, Chongqing University, Chongqing 400044, China

³ Chongqing Institute of New Energy Storage Materials and Equipment, Chongqing 401135, China

* Correspondence: xfy@cqu.edu.cn

Abstract: The commercialization of sodium batteries faces many challenges, one of which is the lack of suitable high-quality separators. Herein, we presented a novel natural silkworm cocoon-derived separator (SCS) obtained from the cocoon inner membrane after a simple degumming process. A Na|Na symmetric cell assembled with this separator can be stably cycled for over 400 h under test conditions of 0.5 mA cm⁻²–0.5 mAh cm⁻². Moreover, the Na|SCS|Na₃V₂(PO₄)₃ full cell exhibits an initial capacity of 79.3 mAh g⁻¹ at 10 C and a capacity retention of 93.6% after 1000 cycles, which far exceeded the 57.5 mAh g⁻¹ and 42.1% of the full cell using a commercial glass fiber separator (GFS). The structural origin of this excellent electrochemical performance lies in the fact that cationic functional groups (such as amino groups) on silkworm proteins can de-solvate Na-ions by anchoring the ClO₄⁻ solvent sheath, thereby enhancing the transference number, transport kinetics and deposition/dissolution properties of Na-ions. In addition, the SCS has significantly better mechanical properties and thinness indexes than the commercial GFS, and, coupled with the advantages of being natural, cheap, non-polluting and degradable, it is expected to be used as a commercialized sodium battery separator material.

Keywords: sodium metal battery; separator materials; natural silkworm cocoon; Na-ion de-solvated function; mechanistic analysis



Citation: Wang, Z.; Zhou, Z.; Gao, X.; Liu, Q.; Man, J.; Du, F.; Xiong, F.

Natural Silkworm Cocoon-Derived Separator with Na-Ion De-Solvated Function for Sodium Metal Batteries.

Molecules **2024**, *29*, 4813. <https://doi.org/10.3390/molecules29204813>

Academic Editor: Chaoji Chen

Received: 26 August 2024

Revised: 3 October 2024

Accepted: 9 October 2024

Published: 11 October 2024



Copyright: © 2024 by the authors. Licensee MDPI, Basel, Switzerland. This article is an open access article distributed under the terms and conditions of the Creative Commons Attribution (CC BY) license (<https://creativecommons.org/licenses/by/4.0/>).

1. Introduction

The growing energy demand has greatly prompted researchers to explore electrochemical energy storage systems (EESs) with low-cost, high energy density and environmental friendliness characteristics [1,2]. Among all available EESs, sodium metal batteries (SMBs) are considered to be the most promising substitutes to Li-ion batteries (LIBs) owing to the following unique advantages [3]: (i) SMBs work similarly to LIBs, so the research experience with LIBs can be utilized to develop SMBs [4]. (ii) Sodium resources are abundant and evenly distributed worldwide, which leads to a potential low cost of sodium metal anodes (SMAs) [5]. (iii) Sodium metal anodes possess low redox potential (−2.71 V vs. the standard hydrogen potential), light weight (23 g mol⁻¹) and high theoretical specific capacity (1166 mAh g⁻¹), endowing SMBs with high working voltage and high energy density [6]. Despite the attractive advantages, the development of SMBs has encountered various bottlenecks, one of which is the lack of high-quality separators [7].

As an important component of battery, the separator, on the one hand, bears the task of isolating the flow of electrons between the cathode and anode within the battery; on the other hand, it is also responsible for allowing ions to pass through smoothly [8]. There is no doubt that the quality of the separator determines the final performance of the battery. Compared to Na-ion batteries, SMBs place a higher demand on the electrolyte

wettability and uptake capability, thermal stability, mechanical strength and ion distribution regulation ability of the separator [9]. Currently, the commercial Na-ion battery utilizes an LIB separator, i.e., a polypropylene (PP) or polyethylene (PE) separator. However, due to the drawbacks such as inferior electrolyte wettability, poor thermal stability and low electrolyte uptake capability, PP/PE separators are unsuitable for SMBs [10]. Although glass fiber separators (GFSs) can solve the above problems and are therefore widely used in laboratory research, their excessive thickness and poor mechanical properties make them difficult to apply in industrial production [11,12].

Scientists have made tremendous efforts to develop high-quality separators for SMBs [13]. Among them, biomass-derived separators have gained increasing attention due to their environmental friendliness, renewability and resource abundance [14]. Casas et al. cross-linked carboxymethyl cellulose (CMC) and hydroxyethyl cellulose (HEC) to prepare membranes with large specific surface area [15]. The Na||Na₃V₂(PO₄)₃(NVP) battery assembled with this biomass membrane as a separator delivered a residual capacity of 74 mAh g^{−1} after 10 cycles at 0.1 C with a nearly 100% Coulombic efficiency, which were both higher than that of the battery using a commercial Whatman GFS (61 mAh g^{−1}, 96%). Wang's group used electrospinning technology to construct cellulose nanocrystals into flexible bifunctional separators and applied them to SMBs [16]. This kind of separator can not only promote the uniform deposition of Na-ions on the anode by regulating the ion flow and nucleation behavior, but can also take advantage of the mechanical strength to block the continuous vertical growth of sodium dendrites, thus avoiding the occurrence of short circuits. These studies confirm the potential of biomass-derived separators for SMB applications and inspire subsequent researchers to continue to delve deeper into the natural treasure trove.

The silkworm cocoon is an amazing biological material that is naturally porous and layered, and therefore has morphological similarities to battery separators. Based on this similarity, silkworm cocoons have been initially developed as separators for LIBs [17–22]. Pereira et al. tested the suitability of silkworm cocoons as LIBs separators in carbonate-based and trifluoromethylsulfonyl-based electrolytes, and the results prove that the former electrolyte is more suitable for LIBs using cocoon separators [17]. In view of the multilayer structure of cocoons, Guo et al. examined the electrochemical performance of sublayers at different positions in cocoons and after stacking, and the results show that the inner layer is more suitable as a separator for LIBs, and the multilayer structure is more beneficial to the electrochemical performance [18]. It is well known that micro-morphology is an important factor affecting the electrochemical performance of the separator, and in order to regulate the pore structure in cocoon-based separators, Reizabal et al. treated cocoons by a salting method [19]. The battery using a cocoon separator with a pore size range of 106–250 µm showed the best electrochemical performance, i.e., a discharge capacity of 66.9 mAh g^{−1} at 2 C and a residual capacity of 56.9 mAh g^{−1} after 55 cycles. In addition to this, the lyophilization [20] and plasma treatment [21] of silk have been used to optimize the morphology of cocoon-based separators with exciting progress.

In this paper, we reported a novel natural silkworm cocoon separator (SCS) for SMBs. The unique advantage of SCSs over commercially available GFSs is that they can anchor ClO₄[−] in the electrolyte by virtue of the abundant amino functional groups in the protein molecular chain, thus enabling Na-ions to exhibit superior transport kinetics. Benefiting from this, the Na||SCS||Na symmetric cell is able to cycle stably for more than 400 h at a current density of 0.5 mA cm^{−2} with an areal capacity of 0.5 mAh cm^{−2}, which far exceeds the effective cycling time (~20 h) of the Na||GFS||Na symmetric cell under the same test conditions. In addition, the Na||SCSs||NVP full cell exhibits a discharge capacity of 79.3 mAh g^{−1} at 10 C with a capacity retention rate of 93.6% after 1000 cycles. In order to facilitate the reader to compare the differences in electrochemical performance between the present work and previous cocoon separator studies, we summarize these findings in Table S1.

2. Results

2.1. Electrochemical Performance

In order to optimize the pore structure of silkworm cocoons and to expose the functional groups on their protein molecules, natural silkworm cocoons were boiled in a weak alkaline solution to remove the sericin [22]. The SCS sample has four broadened crystal diffraction peaks located at 9.1° , 20.5° , 23.0° and 29.4° (Figure 1a). These diffraction peaks should be attributed to the (100), (210), (002) and (300) crystal planes of β -sheet silkworm protein, respectively [23–25]. Table S2 summarizes the structural parameters of each grain surface calculated using Jade 6 software and the Debye–Scherrer formula, where a small grain size (<4 nm) implies the poor crystallinity of the SCS sample [26,27]. In contrast, no crystal diffraction peaks are observed in the XRD patterns of the GFS sample due to the disordered characteristics of glass fiber [28]. Scanning electron microscopy (SEM) was employed to observe the morphology features of the samples at the micron scale [29–31]. As shown in Figure 1b,c, the morphology of the inner and outer layers of the cocoon varies greatly: the silkworm in the outer layer of cocoon is fluffy and stacked with large pores; the silkworm in the inner layer of the cocoon is flat and stacked with small pores, and an obvious bonding phenomenon can be observed. This bonding phenomenon is significantly reduced after boiling (Figure 1d). In view of the advantages in regularity and pore structure, the inner layer of the cocoon was selected as the separator for SMBs. The GFS also exhibits a large pore structure and has no bonding points between its fibers (Figure 1e). The bonding between fibers is likely to be the structural root cause of the superior mechanical properties of the SCS over the GFS [32].

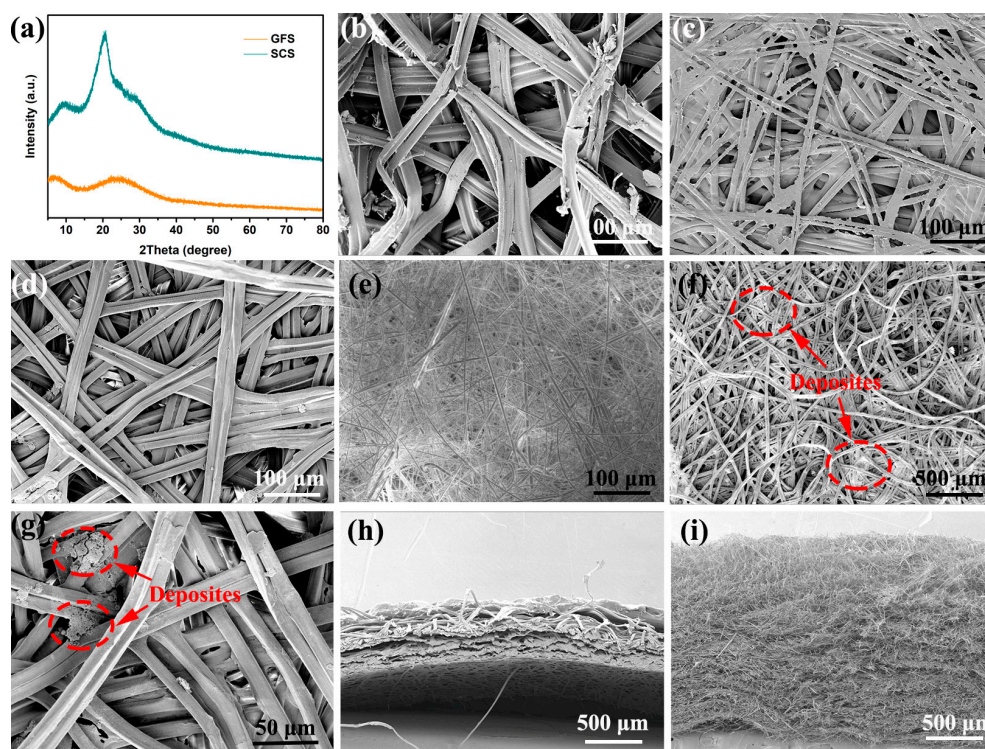


Figure 1. (a) XRD of the SCS and GFS. SEM top view images of the outer layer (b), pristine (c)/boiled (d) inner layers of the cocoon and the glass fiber separator (e). (f,g) SEM images of SCS samples after cyclic testing. SEM cross-section view images of the cocoon (h) and GFS (i).

SEM images of the SCS samples after 100 cycles at 5 C show no significant changes in the SCS except that some deposits can be observed (as shown in Figure 1f,g). Based on previous studies, it is known that these sediments are metallic sodium crystals and sodium salt crystals, of which the former is predominant [33]. In order to evaluate the pore structure of the separators more comprehensively, SEM tests were performed on the cross-sections

of the cocoons and GFS, respectively. As shown in Figure 1h, the cocoons were clearly stratified, with the inner layer being more regular and tightly packed compared to the outer layer, which is consistent with the results observed in Figure 1b,c. The SCS, taken from the inner layer of the cocoon, is much lower than the GFS (Figure 1i) in both porosity and tortuosity.

The Na || Cu asymmetric and Na || Na symmetric cells using SCSs and GFSs as separators were assembled for testing. As shown in Figure S1, the assembled Na || SCS || Cu battery shows a lower nucleation over-potential of 0.065 V than that of the Na || GFS || Cu battery (0.113 V), indicating that the SCS could decrease the nucleation resistance and local current density during Na deposition [34]. Figure 2 presents the voltage–time profiles of Na || Na symmetric cells with the SCS and the GFS. Notably, the Na || SCS || Na symmetric cell can stably cycle for ~480 h and the polarization voltage is stabilized at only 0.04 V throughout under 0.2 mA cm^{−2}–0.2 mAh cm^{−2} test conditions (Figure 2a). As for the Na || GFS || Na battery, the polarization voltage under the same test conditions is close to 0.075 V and short circuit occurs when the battery run for about 100 h. At the test conditions of 0.5 mA cm^{−2}–0.5 mAh cm^{−2}, the Na || SCS || Na symmetric cell exhibits a polarization voltage of ~0.05 V (Figure 2b). After 400 h of steady operation, the polarization voltage of this battery rises slightly to ~0.09 V and eventually fails completely after 427 h of operation. As a comparison, the Na || GFS || Na cell displays an initial polarization voltage as high as 0.125 V and only stably cycles for about 20 h. The above results indicate that SCS is more beneficial as a battery separator for Na-ion transport and deposition/dissolution [35].

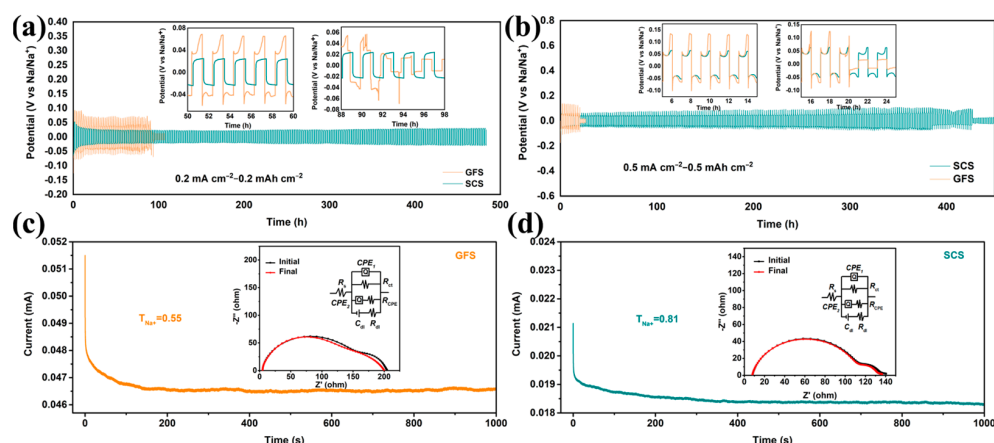


Figure 2. Characterization of sodium plating/stripping behavior in symmetric batteries. Voltage profiles of the symmetrical Na || GFS || Na and Na || SCS || Na cells under current areal capacities of (a) 0.2 mAh cm^{−2} and (b) 0.5 mAh cm^{−2}. The *i*–*t* curves of Na || GFS || Na (c) and Na || SCS || Na (d) cells; the insets are the corresponding EIS curves before and after chronoamperometry test.

To clarify the effect of the SCS on Na-ion transport in batteries, chronoamperometry (CA) and corresponding electrochemical impedance spectroscopy (EIS) tests were performed on the Na || GFS || Na and Na || SCS || Na cells. After careful comparison, all the EIS curves in Figure 2c,d are well matched to the “ $R_s(QR_{ct}(QR_{CPE})(C_{dl}R_{dl}))$ ” equivalent circuit with errors of less than 4.1%. Here, *Q* represents the constant phase element (CPE); *C*_{dl} represents double layer capacitance; and *R*_s, *R*_{ct}, *R*_{CPE} and *R*_{dl} represent solution impedance, charge transfer impedance, CPE impedance and double capacitance impedance, respectively [36,37]. As reported by the ZSimpwin 3.60 software fitting parameter (Table S3), the initial *R*_{ct} of the Na || SCS || Na cell (134.6 Ω) is much smaller than that of the Na || GFS || Na cell (205.7 Ω), indicating that the interfacial impedance between the SCS and the sodium metal anode is smaller. The Na⁺ transference number (*T*_{Na⁺}) of the above symmetric cell can be calculated using the following equation [38,39]:

$$T_{Na^+} = (I_s \times (\Delta V - I_0 \times R_0)) / (I_0 \times (\Delta V - I_s \times R_s))$$

where ΔV , I_0 , I_s , R_0 and R_s are the constant applied voltage (10 mV), initial and steady-state currents, and the R_{ct} before and after the CA test. The calculated T_{Na^+} of the Na||SCS||NVP cell is 0.81, which is higher than the 0.55 of Na||GFS||NVP cell.

To further demonstrate the application potential of SCSs, the electrochemical performances of Na||NVP full batteries using the SCS and the GFS were tested. As shown in Figure 3a,b, the Na||GFS||NVP and Na||SCS||NVP cells exhibit similar electrochemical reaction potentials (~ 3.4 V) and discharge capacities (~ 100 mAh g^{−1}) at 0.1 C. When the charge/discharge rate is increased to 10 C, the Na||SCS||NVP cell still displays a discharge capacity of 79.3 mAh g^{−1}, which is much higher than that of the Na||GFS||NVP cell (60 mAh g^{−1}). It should be noted that the potential hysteresis in the charge–discharge curves of the Na||SCS||NVP cell is only about 1/2 of that of the Na||GFS||NVP cell at 10 C (Figure S2a,b). This phenomenon suggests that Na-ions are able to pass through SCSs more easily and are not over-enriched on the surface of SCSs even at high current densities [40,41]. The rate performance test reveals that the Na||SCS||NVP cell consistently outperforms the Na||GFS||NVP cell in terms of discharge capacity at 0.5–10 C, and the higher the rate, the more pronounced this advantage becomes (Figure 3c). Furthermore, the Na||SCS||NVP cell also exhibits better cycling performance than the Na||GFS||NVP cell at 10 C (Figure 3d). The discharge capacity of the Na||SCS||NVP cell remains 74.2 mAh g^{−1} after 1000 cycles, corresponding to a capacity retention rate of 93.6%. In contrast, the discharge capacity and capacity retention rate of the Na||GFS||NVP cell are only 24.2 and 42.1%, respectively. Moreover, the discharge medium voltage of the full cell using the SCS gradually increases with cycling until it stabilizes near 3.2 V, while that of the full cell using the GFS keeps decreasing (Figure S2c).

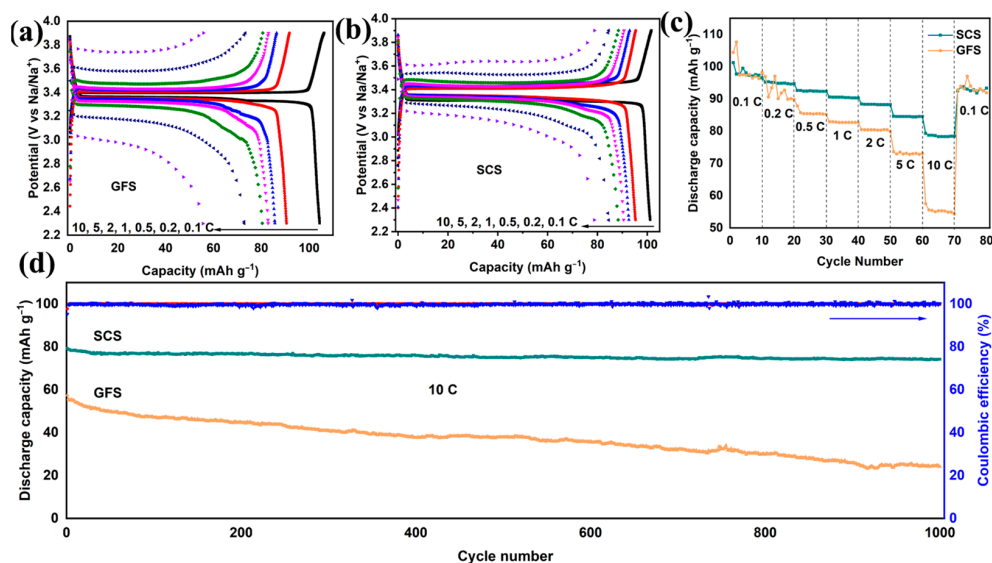


Figure 3. Comparison of electrochemical performances of Na||NVP full cells assembled with SCSs and GFSs. Galvanostatic charging–discharging profile curves of the Na||SCS||NVP (a) and Na||GFS||NVP full cells (b) from 0.1 C to 10 C. Rate capabilities (c) and long-term cycling performances (d) of the Na||SCS||NVP and Na||GFS||NVP full cells.

In order to understand the chemical stability of SCSs during electrochemical reactions, cyclic voltammetry (CV) tests of both the Na||SCS||NVP and Na||GFS||NVP full cells were executed. Compared with the Na||GFS||NVP cell, the Na||SCS||NVP cell also exhibits only a pair of V^{3+}/V^{4+} redox peaks attributed to NVP cathode materials (Figure S3a), which implies that the SCS is in a chemically stable state during electrochemical processes. Electrochemical impedance spectroscopy (EIS) is an efficient testing technique to analyze the internal resistance distribution of a battery. The Na||SCS||NVP and the Na||GFS||NVP share the same EIS graphic characteristics (Figure S3b), i.e., both consist of a semicircle in the high-frequency region and a diagonal line in the low-frequency

region. The semicircle is mainly associated with the R_{ct} [42]. The Na||SCS||NVP cell displays a smaller semicircle diameter than the Na||GFS||NVP cell, indicating that the former has smaller values of R_{ct} than the latter, which implies superior transport kinetics of Na-ions in the former [43]. In addition to this, the diffusion coefficient of Na-ions can be quantitatively calculated using the following equation:

$$D_{Na+} = \frac{R^2 T^2}{2A^2 n^4 F^4 C^2 \sigma^2}$$

Since the parameters R (gas constant, $8.314 \text{ J mol}^{-1} \text{ K}^{-1}$), T (room temperature, 298.15 K), A (area of the electrode, 1.13 cm^2), n (the number of electrons involved in electrochemical reactions, 2), F (Faraday constant, $96485.4 \text{ C mol}^{-1}$) and C (the concentration of Na-ions in the unit cell volume, $6.92 \times 10^{-23} \text{ mol cm}^{-3}$) in the above equations are the same for both the GFS and SCS cells, the Na-ion transport efficiency of these two cells should be inversely related to the σ value. By fitting $-Z' - \omega^{-1/2}$ plots to the straight lines in the low-frequency region of the EIS curves (Figure S3c), it is found that the σ -values for cells using SCSs and GFSs are 684.2 and $740.1 \Omega \text{ s}^{-0.5}$ (see Table S4 for details), respectively, which implies a higher D_{Na+} in the cell using SCSs.

2.2. Mechanical Properties and Functional Group Characterization

The mechanical properties of the separator are not only related to the safety of the battery, but also to whether it can match the winding process for industrial production of the battery. As shown in Figure 4b, the maximum tensile strength of the GFS is only 0.16 MPa which is much lower than the minimum tensile strength value (6.9 MPa) in the winding process, and therefore, the GFS cannot be applied to commercialized column batteries [44]. By comparison, the SCS exhibits a much higher tensile strength (17.72 MPa , Figure 4a) and Young's modulus (64.12 MPa , Figure 4c). In terms of mechanical properties, the SCS has met the basic requirements for commercialized separators.

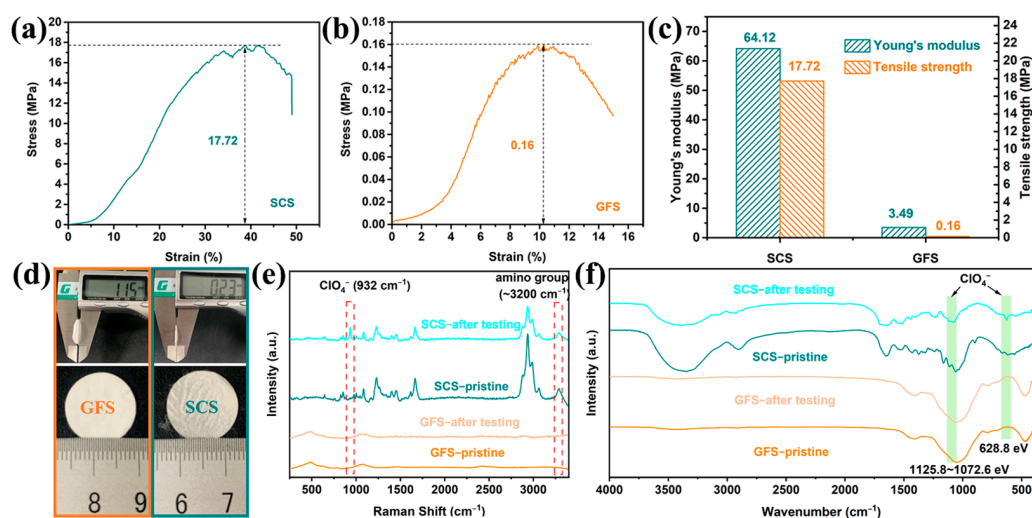


Figure 4. Characterization of mechanical properties and functional groups of the SCS and GFS. Stress–strain curves of the GFS (a) and the SCS (b). (c) Tensile mechanical properties (Young's modulus, strength). (d) Comparison of the appearance and thickness of the SCS and the GFS. (e) Raman and (f) FT-IR spectra of the SCS and the GFS before and after electrochemical reaction.

The appearance characteristics of the GFS and SCS are shown in Figure 4d, and the flatness of the SCS is slightly worse than that of the GFS, which is due to the slight shrinkage of the sample during the drying process of the SCS. The thicknesses of the SCS and GFS are $0.23 \pm 0.01 \text{ mm}$ and $1.15 \pm 0.02 \text{ mm}$, respectively, and the SCS is clearly more advantageous in the demand for a thinner and lighter separator. Raman and FT-IR

spectroscopy were performed on the SCS before and after charging and discharging, respectively. As shown in Figure 4e, a characteristic peak is present at around 3200 cm^{-1} for both SCS samples, which could be attributed to the amino group upon careful comparison with the literature [45]. In addition, the SCS sample after electrochemical testing also exhibits a characteristic peak belonging to ClO_4^- at 932 cm^{-1} that is not found in any other samples [46], suggesting that the SCS sample may anchor the ClO_4^- anion in the electrolyte during the electrochemical reaction. Two sets of characteristic peaks belonging to ClO_4^- at 628.8 and $1125\text{--}1072\text{ cm}^{-1}$ are also observed in the FT-IR spectrum of the SCS after the electrochemical test, reconfirming the inference of a possible interaction between silkworm and ClO_4^- (Figure 4f) [47,48].

It is noteworthy that the XPS spectra also reveal not only the ability of the SCS sample to interact with ClO_4^- but also the presence of amino groups in the silkworm. As shown in Figure 5a, the SCS and GFS exhibit completely different O1s spectra. Specifically, the O1s spectra of the GFS samples before and after the electrochemical reaction did not change significantly, and only one characteristic peak of bridging oxygen was found at 531.5 eV [49]. Meanwhile, the SCS sample has the characteristic peak representing $\text{O}=\text{C}-\text{NH}_2$ at 530.6 eV [50], and the characteristic peaks representing the $\text{Cl}-\text{O}$ (532.1 eV) bond and Na -auger (536.5 eV) are added to the electrochemically reacted SCS sample [51,52]. Combined with the Cl 2p spectrum (Figure 5c), the presence of a ClO_4^- group in the electrochemically reacted SCS sample can be determined [53]. For the C 1s spectra (Figure 5b), three characteristic peaks are observed for the SCS whether it undergoes electrochemical reaction or not, which correspond to a C–C bond at 283.9 eV , a C–COO bond at 285.4 eV and a C–N bond at 287.4 eV [54–56]. In addition, although all samples responded to N 1s spectral detection, the low signal-to-noise ratio of the N 1s spectra of the two GFS samples implies that these samples contain less elemental nitrogen. The high signal-to-noise ratio and good symmetry of the characteristic peaks of the N 1s spectra of the SCS samples indicate that these samples have a high content of nitrogen. The high similarity in the shape and position of the N 1s peaks suggests that the electrochemical reaction does not significantly change the valence state of elemental N.

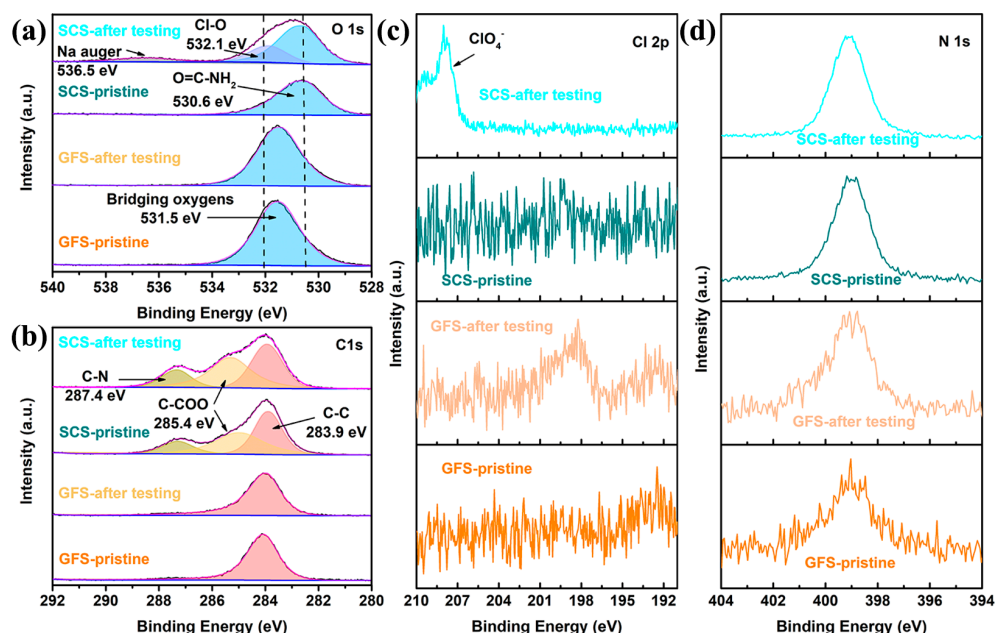


Figure 5. (a) O 1s, (b) C 1s, (c) Cl 2p and (d) N 1s XPS spectra of the GFS and SCS samples.

3. Discussion

The low nucleation over-potential of 0.065 V (Figure S1) and the stable cycling of 427 h under test conditions of 0.5 mA cm^{-2} – 0.5 mAh cm^{-2} (Figure 2b) demonstrate that the Na-

ion deposition/dissolution in SCS-assembled cells is not only easier but also has excellent reversibility [57]. In addition to this, the small charge transfer resistance (Figure S3b) implies excellent transport kinetics of Na-ions in the cell using the SCS [58]. Under the synergistic effect of excellent Na-ion transport and deposition/dissolution kinetics, the batteries using SCSs exhibit superior high-rate cycling performance. Therefore, the Na||SCS||NVP full battery displays an initial capacity of 79.3 mAh g^{-1} at 10 C and a capacity retention of 93.6% after 1000 cycles (Figure 3d), which far exceeds the 57.5 mAh g^{-1} and 42.1% of the Na||GFS||NVP full battery. There is a significant effect of separator thickness on the electrochemical performance and that the thickness of the SCS in this work is much lower than that of the GFS (Figure 4d). In order to clarify the specific effect of separator thickness on electrochemical performance, the commercial GFA separator (only $0.34 \pm 0.01 \text{ mm}$ in thickness), which is thinner than the GFS, was used for a comparison experiment. As shown in Figure S4, the Na||GFA||NVP cell experiences a rapid capacity decline in the multifold test, with the capacity decaying from 115 mAh g^{-1} at 0.1 C to 44 mAh g^{-1} at 5 C until the cell fails at 10 C. The results of this test show that the thinner the separator, the harder it is to obtain excellent electrochemical performance.

Characteristic peaks belonging to ClO_4^- are observed in the Raman (Figure 4e), FT-IR (Figure 4f) and XPS patterns (Figure 5a,c) of the SCS samples after electrochemical testing, which are not observed in the pristine SCS or the GFS before and after electrochemical testing, suggesting that ClO_4^- could be firmly attached to the SCS fibers. Combined with the previous literature, it can be reasonable to assume that this phenomenon is most likely caused by cationic functional groups (such as amino groups) on the protein molecule [59,60]. From the conclusions of previous studies, it is known that Na-ions undergo solvation reactions with anions and solvents during transport in the electrolyte [61,62]. The solvated Na-ions increase in both mass and volume, which undoubtedly reduces the transport kinetics of the Na-ions [63]. As shown in Figure 6, when solvated Na-ions pass through the SCS, the amino functional groups on silkworm proteins disrupt the solvent sheath by anchoring ClO_4^- , thereby releasing free Na-ions. As a result, the transference number ($T_{\text{Na}^+} = 0.81$), transport kinetics and deposition/solvent properties of Na-ions are improved. On this basis, the advantages in mechanical strength and thinness make SCSs more promising than GFSs for commercialized sodium batteries.

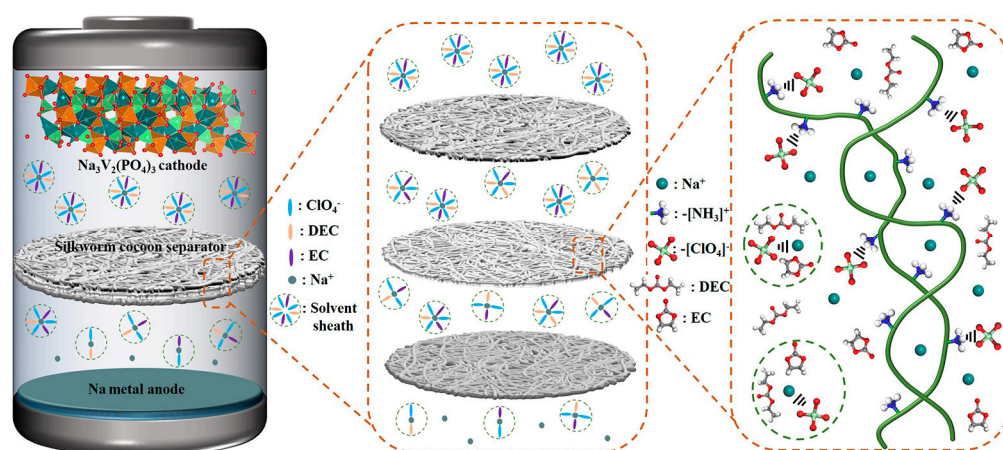


Figure 6. Schematic diagram of the cell structure and the SCS' action mechanism.

4. Materials and Methods

4.1. Fabricating SCS

The SCS fabrication process is shown in Figure 7. First, 0.04 mol Na_2CO_3 (99.8%, Shanghai Macklin Biochemical Technology Co., Ltd., Shanghai, China) was dissolved in 2 L deionized water to prepare the washing solution and heated to boiling. The mulberry silkworm cocoons (Beijing Tong Ren Tang group Co., Ltd., Beijing, China) were then poured into the boiling liquid and treated for 20 min to remove the sericin. Next, the cocoons were

fished out, washed three times with deionized water and exfoliated of their inner layers. Subsequently, the inner layer of the cocoon was flattened, sandwiched between two glass plates to fix the shape, and transferred to a vacuum oven at 80 °C until dry. The dried cocoons' inner layer was cut into 16 mm discs to be used as separators, which were named SCS. Thick (Whatman GF/D) and thin (Whatman GF/A) glass fiber separators were used as comparison samples, named GFS and GFA, respectively.

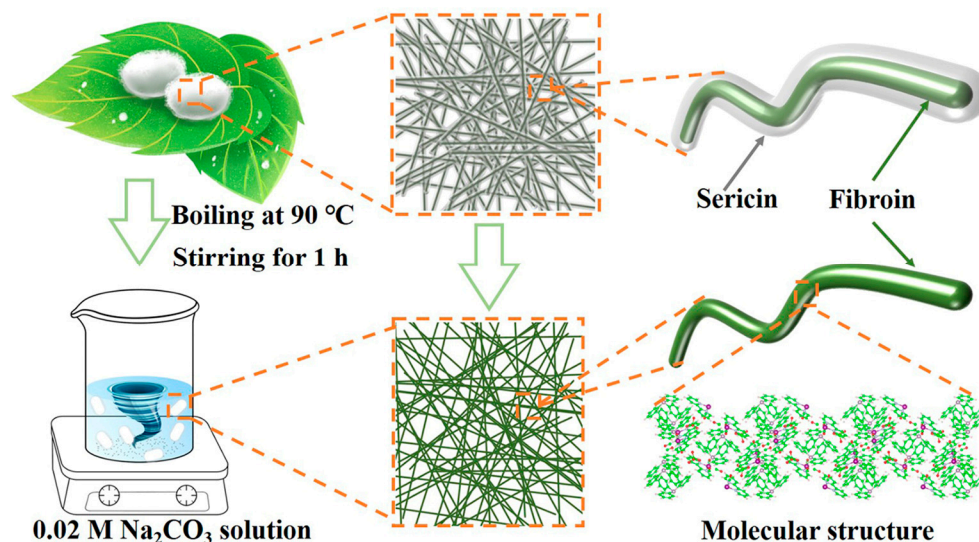


Figure 7. Schematic diagram of the preparation process of silkworm cocoon separator.

4.2. Material Characterization

The microscopic morphology of the SCS, GFS and sodium metal anode was observed by field-emission scanning electron microscopy (FESEM, Thermo Fisher Scientific FIB-SEM GX4, Waltham, MA, USA). The XRD data were measured by a Bruker D8 diffractometer at a sweep speed of $0.3^{\circ} \text{ s}^{-1}$ over a range of $5\text{--}80^{\circ}$ with $\text{Cu K}\alpha$ ($\lambda = 1.5418 \text{ \AA}$). FT-IR absorption spectroscopy (Thermo Scientific Nicolet iS50, Waltham, MA, USA) was used to test the functional groups of different separators in the range of $600 \text{ cm}^{-1}\text{--}4000 \text{ cm}^{-1}$; all samples were washed three times in water under sonication for 10 min before testing. An electronic universal testing machine was employed to test the mechanical properties of different separators. An X-ray photoelectron spectrometer (ThermoFischer, ESCALAB 250Xi, Waltham, MA, USA) was used in this experiment for XPS tests. In this case, the vacuum of the analysis chamber was $2 \times 10^{-8} \text{ Pa}$, the excitation source was an $\text{Al K}\alpha$ ray ($h\nu = 1486.6 \text{ eV}$) and the operating voltage was 12.5 kV. Raman spectroscopy tests were performed on a ThermoFischer Dxr3xi Raman microscopy (Waltham, MA, USA) instrument equipped with an Ar^{+} laser ($\lambda = 532 \text{ nm}$).

4.3. Electrochemical Measurements

All the electrochemical performance tests were performed based on CR2025-type coin batteries, and the battery assembly was completed in an argon-filled glovebox ($\text{H}_2\text{O} < 0.1 \text{ ppm}$, $\text{O}_2 < 0.1 \text{ ppm}$, Mikrouna, Shanghai, China). For the preparation of the NVP cathode, NVP (Guangdong Canrd New Energy Technology Co., Ltd., Dongguan, China), polyvinylidene fluoride (PVDF) and acetylene black with a mass ratio of 8:1:1 were dispersed in N-methyl-2-pyrrolidone (NMP) to form a uniform slurry and then coated on aluminum foils. After they were dried in a vacuum oven at 110°C for 10 h, these aluminum foils were cut into discs with a diameter of 14 mm to be the NVP cathode. An amount of $50 \mu\text{L}$ of electrolytes (1 M NaClO_4 dissolved in $\text{EC}:\text{DEC}=1:1$ (v/v) with 5% FEC) was used for each battery. All batteries used Na foil ($\sim 100 \mu\text{m}$) as the anode, and the difference was that the working electrodes were NVP, Cu foil or Na foil, with the GFS or SCS as the separator. The galvanostatic charging–discharging, over-potential and cycling performance of the

batteries were measured on a Land BT 2000 battery test systems at 25 °C. The potentiostatic modal EIS (frequency range from 10^{-2} to 10^5 Hz with an amplitude value of 10 mV), CV (voltage range from 2.3 to 3.9 V with a scanning rate of 0.1 mV s^{-1}) and CA (open-circuit voltage used as initial voltage, executed for 1000 s at 10 mV bias) curves were tested on a CHI660e electrochemical workstation.

5. Conclusions

In summary, we developed a novel natural SCS for sodium metal batteries. Systematic structural characterization reveals that the cationic functional groups (such as amino groups) enriched in the SCS samples can anchor the ClO_4^- solvent sheath around the Na^+ ions, realizing a high Na^+ transference number ($T_{\text{Na}^+} = 0.81$) and substantially enhancing the transport kinetics. Benefiting from this, the $\text{Na}||\text{SCS}||\text{Na}$ symmetric cell can be stably cycled for over 400 h at 0.5 mA cm^{-2} – 0.5 mAh cm^{-2} . Moreover, the $\text{Na}||\text{SCS}||\text{NVP}$ full battery displays a reversible discharge specific capacity of 79.3 mAh g^{-1} at 10 C and a remaining capacity of up to 74.2 mAh g^{-1} after 1000 cycles. In addition, the mechanical properties and thickness of the SCS are also completely superior to those of the GFS, which means that the SCS has more potential for commercial application than the GFS.

Supplementary Materials: The following supporting information can be downloaded at <https://www.mdpi.com/article/10.3390/molecules29204813/s1>: Figure S1: Voltage-capacity curves of $\text{Cu}||\text{SCS}||\text{Na}$ and $\text{Cu}||\text{GFS}||\text{Na}$ asymmetric cell at a current density of 0.5 mA cm^{-2} ; Figure S2: Charge-discharge voltage profiles for $\text{Na}||\text{NVP}$ full batteries using GFS (a) and SCS (b) separator. The discharge medium voltage at different cycles of $\text{Na}||\text{GFS}||\text{NVP}$ and $\text{Na}||\text{SCS}||\text{NVP}$ full batteries; Figure S3: (a) CV curves at a scan rate of 0.1 mV s^{-1} , (b) EIS curves (inset: equivalent circuit diagram) and (c) relationship plots of the impedance as a function of the inverse square root of angular frequency in a low-frequency region of $\text{Na}||\text{SCS}||\text{NVP}$ and $\text{Na}||\text{GFS}||\text{NVP}$ full cells; Figure S4: Galvanostatic charging-discharging profile curves of $\text{Na}||\text{GFA}||\text{NVP}$; Table S1: Comparative table of electrochemical properties of cocoon based separators; Table S2: Summary table of structural parameters of SCS sample; Table S3: Parameters reported for EIS curves in Figure 2c,d fitted by equivalent circuits. Table S4: Parameters reported of the EIS curves in Figure S3 after equivalent circuits and linear fitting.

Author Contributions: Conceptualization, Z.W. and F.X.; methodology, Z.Z.; validation, X.G. and Q.L.; investigation, X.G.; data curation, Z.Z. and Q.L.; writing—original draft preparation, Z.Z., X.G. and Q.L.; writing—review and editing, Z.W., J.M., F.D. and F.X.; funding acquisition, Z.W. All authors have read and agreed to the published version of the manuscript.

Funding: This research was funded by the PhD Initiation Program of Liaocheng University, grant number 318052012, and the Open Project Program of Shandong Provincial Key Laboratory of Chemical Energy Storage and Novel Cell Technology, Liaocheng University, China.

Institutional Review Board Statement: Not applicable.

Informed Consent Statement: Not applicable.

Data Availability Statement: The data that support the findings of this study are available from the corresponding author upon reasonable request.

Acknowledgments: The authors acknowledge Liaocheng University for the financial support.

Conflicts of Interest: The authors declare no conflicts of interest.

References

1. Huang, X.Z.; He, R.; Li, M.; Chee, M.O.L.; Dong, P.; Lu, J. Functionalized separator for next-generation batteries. *Mater. Today* **2020**, *41*, 143–155. [CrossRef]
2. Lizundia, E.; Kundu, D. Advances in natural biopolymer-based electrolytes and separators for battery applications. *Adv. Funct. Mater.* **2021**, *31*, 2005646. [CrossRef]
3. Sullivan, M.; Tang, P.; Meng, X.B. Atomic and molecular layer deposition as surface engineering techniques for emerging alkali metal rechargeable batteries. *Molecules* **2022**, *27*, 6170. [CrossRef]
4. Lie, C. Sustainable battery materials from biomass. *ChemSusChem* **2020**, *13*, 2110–2141.

5. Vaalma, C.; Buchholz, D.; Weil, M.; Passerini, S. A cost and resource analysis of sodium-ion batteries. *Nat. Rev. Mater.* **2018**, *3*, 18013. [\[CrossRef\]](#)
6. Lee, B.; Paek, E.; Mitlin, D.; Lee, S.W. Sodium metal anodes: Emerging solutions to dendrite growth. *Chem. Rev.* **2019**, *119*, 5416–5460. [\[CrossRef\]](#)
7. Li, Y.C.; Fu, X.W.; Wang, Y.; Zhong, W.H.; Li, R.F. “See” the invisibles: Inspecting battery separator defects via pressure drop. *Energy Storage Mater.* **2019**, *16*, 589–596. [\[CrossRef\]](#)
8. Lagadec, M.F.; Zahn, R.; Wood, V. Characterization and performance evaluation of lithium-ion battery separators. *Nat. Energy* **2018**, *4*, 16–25. [\[CrossRef\]](#)
9. Wang, J.M.; Gao, Y.; Liu, D.; Zou, G.D.; Li, L.J.; Fernandez, C.; Zhang, Q.R.; Peng, Q.M. A sodiophilic amyloid fibril modified separator for dendrite-free sodium-metal batteries. *Adv. Mater.* **2024**, *36*, 2304942. [\[CrossRef\]](#)
10. Zhang, L.P.; Li, X.L.; Yang, M.R.; Chen, W.H. High-safety separators for lithium-ion batteries and sodium-ion batteries: Advances and perspective. *Energy Storage Mater.* **2021**, *41*, 522–545. [\[CrossRef\]](#)
11. Zhu, J.D.; Yanilmaz, M.; Fu, K.; Chen, C.; Lu, Y.; Ge, Y.Q.; Kim, D.; Zhang, X.W. Understanding glass fiber membrane used as a novel separator for lithium–sulfur batteries. *J. Membr. Sci.* **2016**, *504*, 89–96. [\[CrossRef\]](#)
12. Zhang, X.Y.; Cheng, S.A.; Huang, X.; Logan, B.E. The use of nylon and glass fiber filter separators with different pore sizes in air-cathode single-chamber microbial fuel cells. *Energy Environ. Sci.* **2010**, *3*, 659–664. [\[CrossRef\]](#)
13. Liu, Z.F.; Jiang, Y.J.; Hu, Q.M.; Guo, S.T.; Yu, L.; Li, Q.; Liu, Q.; Hu, X.L. Safer lithium-ion batteries from the separator aspect: Development and future perspectives. *Energy Environ. Mater.* **2021**, *4*, 336–362. [\[CrossRef\]](#)
14. Jin, C.B.; Nai, J.W.; Sheng, O.W.; Yuan, H.D.; Zhang, W.K.; Tao, X.Y.; Lou, X.W. Biomass-based materials for green lithium secondary batteries. *Energy Environ. Sci.* **2021**, *14*, 1326. [\[CrossRef\]](#)
15. Casas, X.; Niederberger, M.; Lizundia, E. A sodium-ion battery separator with reversible voltage response based on water-soluble cellulose derivatives. *ACS Appl. Mater. Interfaces* **2020**, *12*, 29264–29274. [\[CrossRef\]](#)
16. Wang, J.; Xu, Z.; Zhang, Q.C.; Song, X.; Lu, X.K.; Zhang, Z.Y.; Onyianta, A.J.; Wang, M.N.; Titirici, M.M.; Eichhorn, S.J. Stable sodium-metal batteries in carbonate electrolytes achieved by bifunctional, sustainable separators with tailored alignment. *Adv. Mater.* **2022**, *34*, 2206367. [\[CrossRef\]](#)
17. Reizabal, A.; Fidalgo-Marijuan, A.; Gonçalves, R.; Gutiérrez-Pardo, A.; Aguesse, F.; Pérez-Álvarez, L.; Vilas-Vilela, J.L.; Costa, C.M.; Lanceros-Mendez, S. Silk-fibroin and sericin polymer blends for sustainable battery separators. *J. Colloid Interface Sci.* **2022**, *611*, 366–376. [\[CrossRef\]](#)
18. Guo, X.S.; Li, J.Y.; Xing, J.X.; Zhang, K.; Zhou, Y.G.; Pan, C.; Wei, Z.Z.; Zhao, Y. Silkworm cocoon layer with gradient structure as separator for lithium-ion battery. *Energy Technol.* **2022**, *10*, 2100996. [\[CrossRef\]](#)
19. Reizabal, A.; Gonçalves, R.; Fidalgo-Marijuan, A.; Costa, C.M.; Pérez, L.; Vilas, J.-L.; Lanceros-Mendez, S. Tailoring silk fibroin separator membranes pore size for improving performance of lithium ion batteries. *J. Membr. Sci.* **2020**, *598*, 117678. [\[CrossRef\]](#)
20. Pereira, R.F.P.; Brito-Pereira, R.; Gonçalves, R.; Silva, M.P.; Costa, C.M.; Silva, M.M.; Bermudez, V.D.Z.; Lanceros-Méndez, S. Silk fibroin separators: A step towards lithium ion batteries with enhanced sustainability. *ACS Appl. Mater. Interfaces* **2018**, *10*, 5385–5394. [\[CrossRef\]](#)
21. Pereira, R.F.P.; Gonçalves, R.; Gonçalves, H.M.R.; Correia, D.M.; Costa, C.M.; Silva, M.M.; Lanceros-Méndez, S.; Bermudez, V.D.Z. Plasma-treated Bombyx mori cocoon separators for high-performance and sustainable lithium-ion batteries. *Mater. Today Sustain.* **2020**, *9*, 100041. [\[CrossRef\]](#)
22. Biswal, B.; Dan, A.K.; Sengupta, A.; Das, M.; Bindhani, B.K.; Das, D.; Parhi, P.K. Extraction of silk fibroin with several sericin removal processes and its importance in tissue engineering: A review. *J. Polym. Environ.* **2022**, *30*, 2222–2253. [\[CrossRef\]](#)
23. Chen, X.D.; Wang, Y.F.; Wang, Y.J.; Li, Q.Y.; Liang, X.Y.; Wang, G.; Li, J.L.; Peng, R.J.; Sima, Y.H.; Xu, S.Q. Ectopic expression of sericin enables efficient production of ancient silk with structural changes in silkworm. *Nat. Commun.* **2023**, *13*, 6295. [\[CrossRef\]](#)
24. Drummy, L.F.; Farmer, B.L.; Naik, R.R. Correlation of the β -sheet crystal size in silk fibers with the protein amino acid sequence. *Soft Matter* **2007**, *3*, 877–882. [\[CrossRef\]](#)
25. Cho, S.Y.; Yun, Y.S.; Lee, S.; Jang, D.; Park, K.Y.; Kim, J.K.; Kim, B.H.; Kang, K.; Kaplan, D.L.; Jin, H.J. Carbonization of a stable β -sheet-rich silk protein into a pseudographitic pyroprotein. *Nat. Commun.* **2015**, *6*, 7145. [\[CrossRef\]](#) [\[PubMed\]](#)
26. Dash, P.; Yang, J.M.; Lin, H.; Lin, A.S. Preparation and characterization of zinc gallate phosphor for electrochemical luminescence. *J. Lumin.* **2020**, *228*, 117593. [\[CrossRef\]](#)
27. Ding, Z.; Li, H.; Shaw, L. New insights into the solid-state hydrogen storage of nanostructured $\text{LiBH}_4\text{-MgH}_2$ system. *Chem. Eng. J.* **2020**, *385*, 123856. [\[CrossRef\]](#)
28. Liu, Y.J.; Tai, Z.X.; Rozen, I.; Yu, Z.P.; Lu, Z.Y.; LaGrow, A.P.; Bondarchuk, O.; Chen, Q.Q.; Goobes, G.; Li, Y.; et al. Ion flux regulation through PTFE nanospheres impregnated in glass fiber separators for long-lived lithium and sodium metal batteries. *Adv. Energy Mater.* **2023**, *13*, 2204420. [\[CrossRef\]](#)
29. Ding, Z.; Li, Y.T.; Yang, H.; Lu, Y.F.; Tan, J.; Li, J.B.; Li, Q.; Chen, Y.A.; Shaw, L.L.; Pan, F.S. Tailoring MgH_2 for hydrogen storage through nanoengineering and catalysis. *J. Magnes. Alloys* **2022**, *10*, 2946–2967. [\[CrossRef\]](#)
30. Li, Y.T.; Guo, Q.F.; Ding, Z.; Jiang, H.; Yang, H.; Du, W.J.; Zheng, Y.; Huo, K.F.; Shaw, L.L. MOFs-based materials for solid-state hydrogen storage: Strategies and perspectives. *Chem. Eng. J.* **2024**, *485*, 149665. [\[CrossRef\]](#)
31. Yang, H.; Ding, Z.; Li, Y.-T.; Li, S.-Y.; Wu, P.-K.; Hou, Q.-H.; Zheng, Y.; Gao, B.; Huo, K.-F.; Du, W.-J.; et al. Recent advances in kinetic and thermodynamic regulation of magnesium hydride for hydrogen storage. *Rare Met.* **2023**, *42*, 2906–2927. [\[CrossRef\]](#)

32. Nurazzi, N.M.; Asyraf, M.R.M.; Fatimah Athiyah, S.; Shazleen, S.S.; Rafiqah, S.A.; Harussani, M.M.; Kamarudin, S.H.; Razman, M.R.; Rahmah, M.; Zainudin, E.S.; et al. A review on mechanical performance of hybrid natural fiber polymer composites for structural applications. *Polymers* **2021**, *13*, 2170. [\[CrossRef\]](#) [\[PubMed\]](#)
33. Ma, X.H.; Cheng, Z.Y.; Zhang, T.W.; Zhang, X.Q.; Ma, Y.; Guo, Y.Q.; Wang, X.Y.; Zheng, Z.H.; Hou, Z.G.; Zi, Z.F. High efficient recycling of glass fiber separator for sodium-ion batteries. *Ceram. Int.* **2023**, *49*, 23598–23604. [\[CrossRef\]](#)
34. Li, M.H.; Lu, G.J.; Zheng, W.K.; Zhao, Q.N.; Li, Z.P.; Jiang, X.P.; Yang, Z.G.; Li, Z.Y.; Qu, B.H.; Xu, C.H. Multifunctionalized safe separator toward practical sodium-metal batteries with high-performance under high mass loading. *Adv. Funct. Mater.* **2023**, *33*, 2214759. [\[CrossRef\]](#)
35. Hou, J.R.; Xu, T.T.; Wang, B.Y.; Yang, H.Y.; Wang, H.; Kong, D.Z.; Lyu, L.L.; Li, X.J.; Wang, Y.; Xu, Z.L. Self-confinement of Na metal deposition in hollow carbon tube arrays for ultrastable and high-power sodium metal batteries. *Adv. Funct. Mater.* **2024**, *34*, 2312750. [\[CrossRef\]](#)
36. Gannon, W.J.F.; Dunnill, C.W. Apparent disagreement between cyclic voltammetry and electrochemical impedance spectroscopy explained by time-domain simulation of constant phase elements. *Int. J. Hydrogen Energy* **2020**, *45*, 22383–22393. [\[CrossRef\]](#)
37. Xiong, F.Y.; Li, J.T.; Zuo, C.L.; Zhang, X.L.; Tan, S.S.; Jiang, Y.L.; An, Q.Y.; Chu, P.K.; Mai, L.Q. Mg-doped $\text{Na}_4\text{Fe}_3(\text{PO}_4)_2(\text{P}_2\text{O}_7)/\text{C}$ composite with enhanced intercalation pseudocapacitance for ultra-stable and high-rate sodium-ion storage. *Adv. Funct. Mater.* **2023**, *33*, 2211257. [\[CrossRef\]](#)
38. Bruce, P.G.; Vincent, C.A. Steady state current flow in solid binary electrolyte cells. *J. Electroanal. Chem.* **1987**, *225*, 1–17. [\[CrossRef\]](#)
39. Evans, J.; Vincent, C.A.; Bruce, P.G. Electrochemical measurement of transference numbers in polymer electrolytes. *Polymer* **1987**, *28*, 2324–2328. [\[CrossRef\]](#)
40. Wei, Q.L.; Chang, X.Q.; Wang, J.; Huang, T.Y.; Huang, X.J.; Yu, J.Y.; Zheng, H.F.; Chen, J.H.; Peng, D.L. An ultrahigh-power mesocarbon microbeads| Na^+ -diglyme| $\text{Na}_3\text{V}_2(\text{PO}_4)_3$ sodium-ion battery. *Adv. Mater.* **2022**, *34*, 2108304. [\[CrossRef\]](#)
41. Cao, J.L.; Wang, Y.; Wang, L.; Yu, F.; Ma, J. $\text{Na}_3\text{V}_2(\text{PO}_4)_3/\text{C}$ as faradaic electrodes in capacitive deionization for high performance desalination. *Nano Lett.* **2019**, *19*, 823–828. [\[CrossRef\]](#) [\[PubMed\]](#)
42. Panda, P.K.; Cho, T.S.; Hsieh, C.T.; Yang, P.C. Cobalt- and copper-doped NASICON-type LATP polymer composite electrolytes enabling lithium titania electrode for solid-state lithium batteries with high-rate capability and excellent cyclic performance. *J. Energy Storage* **2024**, *95*, 112559. [\[CrossRef\]](#)
43. Huang, R.; Yan, D.; Zhang, Q.Y.; Zhang, G.W.; Chen, B.B.; Yang, H.Y.; Yu, C.Y.; Bai, Y. Unlocking charge transfer limitation in NASICON structured $\text{Na}_3\text{V}_2(\text{PO}_4)_3$ cathode via trace carbon incorporation. *Adv. Energy Mater.* **2024**, *14*, 2400595. [\[CrossRef\]](#)
44. Huang, X.S. A lithium-ion battery separator prepared using a phase inversion process. *J. Power Sources* **2012**, *216*, 216–221. [\[CrossRef\]](#)
45. Berger, E.; Niemelä, J.; Lampela, O.; Juffer, A.H.; Komsa, H.P. Raman spectra of amino acids and peptides from machine learning polarizabilities. *J. Chem. Inf. Model.* **2024**, *64*, 4601–4612. [\[CrossRef\]](#) [\[PubMed\]](#)
46. Sun, Y.L.; Ji, X.; Wang, X.; He, Q.F.; Dong, J.C.; Le, J.B.; Li, J.F. Visualization of electrooxidation on palladium single crystal surfaces via situ Raman spectroscopy. *Angew. Chem. Int. Ed.* **2024**, e202408736. [\[CrossRef\]](#)
47. Yu, J.M.; Guo, T.L.; Wang, C.; Shen, Z.H.; Dong, X.Y.; Li, S.H.; Zhang, H.G.; Lu, Z.D. Engineering two-dimensional metal–organic framework on molecular basis for fast Li^+ conduction. *Nano Lett.* **2021**, *21*, 5805–5812. [\[CrossRef\]](#) [\[PubMed\]](#)
48. Shen, L.; Bin Wu, H.; Liu, F.; Brosmer, J.L.; Shen, G.; Wang, X.; Zink, J.I.; Xiao, Q.; Cai, M.; Wang, G.; et al. Creating lithium-ion electrolytes with biomimetic ionic channels in metal–organic frameworks. *Adv. Mater.* **2018**, *30*, 1707476. [\[CrossRef\]](#)
49. Harizanov, R.; Tashava, T.; Gaydarov, V.; Avramova, I.; Lilova, V.; Nedev, S.; Zamfirova, G.; Nedkova-Shtipska, M.; Rüssel, C. Structure and physicochemical characteristics of the glasses in the system $\text{Na}_2\text{O}/\text{BaO}/\text{ZrO}_2/\text{TiO}_2/\text{SiO}_2/\text{B}_2\text{O}_3/\text{Al}_2\text{O}_3$ -Influence of the ZrO_2 addition on the physico-chemical and mechanical properties. *Solid State Sci.* **2024**, *151*, 107515. [\[CrossRef\]](#)
50. Hurisso, B.B.; Lovelock, K.R.J.; Licence, P. Amino acid-based ionic liquids: Using XPS to probe the electronic environment via binding energies. *Phys. Chem. Chem. Phys.* **2011**, *13*, 17737–17748. [\[CrossRef\]](#)
51. Martin-Vosshage, D.; Chowdari, B.V.R. XPS studies on $(\text{PEO})_n\text{LiClO}_4$ and $(\text{PEO})_n\text{Cu}(\text{ClO}_4)_2$ polymer electrolytes. *J. Electrochem. Soc.* **1995**, *142*, 1442. [\[CrossRef\]](#)
52. Zhou, X.Z.; Chen, X.M.; Yang, Z.; Liu, X.H.; Hao, Z.Q.; Jin, S.; Zhang, L.H.; Wang, R.; Zhang, C.F.; Li, L.; et al. Anion receptor weakens ClO_4^- solvation for high-temperature sodium-ion batteries. *Adv. Funct. Mater.* **2024**, *34*, 2302281. [\[CrossRef\]](#)
53. Amin, M.A. Metastable and stable pitting events on Al induced by chlorate and perchlorate anions-Polarization, XPS and SEM studies. *Electrochim. Acta* **2009**, *54*, 1857–1863. [\[CrossRef\]](#)
54. Sreedhar, B.; Sairam, M.; Chattopadhyay, D.K.; Mitra, P.P.; Rao, D.V.M. Thermal and XPS studies on polyaniline salts prepared by inverted emulsion polymerization. *J. Appl. Polym. Sci.* **2006**, *101*, 499–508. [\[CrossRef\]](#)
55. Stevens, J.S.; Luca, A.C.D.; Pelendritis, M.; Terenghi, G.; Downes, S.; Schroeder, S.L.M. Quantitative analysis of complex amino acids and RGD peptides by X-ray photoelectron spectroscopy (XPS). *Surf. Interface Anal.* **2013**, *45*, 1238–1246. [\[CrossRef\]](#)
56. Tan, S.S.; Jiang, Y.L.; Ni, S.Y.; Wang, H.; Xiong, F.Y.; Cui, L.M.; Pan, X.L.; Tang, C.; Rong, Y.G.; An, Q.Y.; et al. Serrated lithium fluoride nanofibers-woven interlayer enables uniform lithium deposition for lithium-metal batteries. *Natl. Sci. Rev.* **2022**, *9*, nwac183. [\[CrossRef\]](#)
57. Sun, B.; Li, P.; Zhang, J.Q.; Wang, D.; Munroe, P.; Wang, C.Y.; Notten, P.H.L.; Wang, G.X. Dendrite-free sodium-metal anodes for high-energy sodium-metal batteries. *Adv. Mater.* **2018**, *30*, 1801334. [\[CrossRef\]](#)

58. Wang, Z.Y.; Du, Z.J.; Li, Z.; Zhang, X.H.; Liu, J.T.; Dai, Y.H.; Zhang, W.; Wang, D.; Wang, Y.Y.; Li, H.X.; et al. Super-lattices enabled performances of vanadate-phosphate glass-ceramic composite cathode in lithium-ion batteries. *Ceram. Int.* **2024**, *50*, 15407–15416. [[CrossRef](#)]
59. Fu, X.W.; Hurlock, M.J.; Ding, C.F.; Li, X.Y.; Zhang, Q.; Zhong, W.H. MOF-enabled ion-regulating gel electrolyte for long-cycling lithium metal batteries under high voltage. *Small* **2022**, *18*, 2106225. [[CrossRef](#)]
60. Zhu, F.L.; Bao, H.F.; Wu, X.S.; Tao, Y.L.; Qin, C.; Su, Z.M.; Kang, Z.H. High-performance metal–organic framework-based single ion conducting solid-state electrolytes for low-temperature lithium metal batteries. *ACS Appl. Mater. Interfaces* **2019**, *11*, 43206–43213. [[CrossRef](#)]
61. Sheng, L.; Wang, Q.Q.; Liu, X.; Cui, H.; Wang, X.L.; Xu, Y.L.; Li, Z.L.; Wang, L.; Chen, Z.H.; Xu, G.L.; et al. Suppressing electrolyte–lithium metal reactivity via Li^+ -desolvation in uniform nano-porous separator. *Nat. Commun.* **2022**, *13*, 172. [[CrossRef](#)] [[PubMed](#)]
62. Chang, Z.; Qiao, Y.; Deng, H.; Yang, H.J.; He, P.; Zhou, H.S. A liquid electrolyte with de-solvated lithium ions for lithium-metal battery. *Joule* **2020**, *4*, 1776–1789. [[CrossRef](#)]
63. Ma, W.H.; Wang, S.; Wu, X.W.; Liu, W.W.; Yang, F.; Liu, S.D.; Jun, S.C.; Dai, L.; He, Z.X.; Zhang, Q.B. Tailoring desolvation strategies for aqueous zinc-ion batteries. *Energy Environ. Sci.* **2024**, *17*, 4819–4846. [[CrossRef](#)]

Disclaimer/Publisher’s Note: The statements, opinions and data contained in all publications are solely those of the individual author(s) and contributor(s) and not of MDPI and/or the editor(s). MDPI and/or the editor(s) disclaim responsibility for any injury to people or property resulting from any ideas, methods, instructions or products referred to in the content.